Section S1

25

Section 2.1 states that "The IOD term is not lagged, since the GMST anomaly found from a regression that removes the contribution of all other natural and anthropogenic factors exhibits strongest correlation with the IOD index at zero lag time". We use the 50th percentile modelled GMST from a model simulation where IOD was removed as a regressor, which we subtract from the observed GMST to obtain a time series of residuals. The square of the correlation coefficient (R^2) between these residuals and the lagged COBE2 IOD index used in our study (Sect. 2.2.3) is shown in Fig. S1, over 1851–2019 (Fig. S1a) and 1940–2019 (Fig. S1b). The former time period matches the one that is used for the computation of χ^2_{ATM} (Sect. 2.1.2), except for the year 1850, while the latter time period matches the timeframe that is used for the computation of χ^2_{RECENT} .

Section 2.2.6 states that "the time series for the uncertainty in the observed OHC is based on the 1σ uncertainty computed from the five datasets". Using five OHC anomaly records (Levitus et al., 2012; Balmaseda et al., 2013; Ishii et al., 2017; Carton et al., 2018; Cheng et al., 2024), we compute an annual average OHC anomaly time series for the 1955 - 2024 period, which we then normalize to 1989. The year 1989 was chosen for this purpose, as this is the midway point of the 1955 to 2024 period. To obtain an uncertainty time series for our average OHC dataset, we use the 1σ standard deviation, computed from the five OHC datasets, at a given time, or the value of the average standard deviation across the 1955 - 2024 time period, whichever the greater. The average standard deviation between 1955 - 2024 is computed from the time series of the 1σ standard deviations. From this average, we exclude the years 1988 to 1990, as these years have low values of standard deviation due to the OHC anomalies having been normalized to 1989. The use of the long-term mean uncertainty to construct the OHC uncertainty time series eliminates the low values of uncertainty in the late 1980s and early 1990s, which are an artifact of the datasets having been normalized to 1989. Figure S2 shows the five OHC datasets (colors) used to construct our composite OHC dataset (black), and the corresponding uncertainty time series (gray shading). Further information regarding our formulation of OHC, and the use of the reduced χ^2 metric for OHC, is given in Hope et al., (2020) and McBride et al., (2021).

As described in Sect. 2.1.2, we scale the time series of ERF_{AER} by a constant multiplicative factor (s in Eq. (5)) to obtain an ensemble of ERF_{AER} trajectories. The ERF adjustment from IMO2020 is added to each time series for ERF_{AER} after this scaling occurs.

Figure S3 shows the values of Effective Climate Sensitivity (EffCS) as the function of climate feedback and ERF_{AER}. Figure S3 is similar to Fig. 2 in the main paper, which shows computed values of AAWR in the same coordinate system. Colored regions correspond to ensemble members that satisfy all three reduced χ^2 observational constraints, with the colors corresponding to values of EffCS as indicated by the color bars to the right. The model setup used for the simulations in the main paper corresponds to an EffCS of 2.63 °C [1.77 to 3.55 °C, 5–95% range]. These values are generally consistent with, albeit slightly higher than the estimate of 2.29 °C [1.54 to 3.11 °C] obtained with an earlier version of EM–GC in Farago et al., (2025), which was found to be well-aligned with recent estimates of EffCS from literature.

Figures S4 and S5 show the EM-GC model output for the nine benchmark simulations that were used to test the sensitivity of the two-layer EBM to the heat capacities of the upper and lower layers (Appendix A). Panels differ in the equivalent depth of the upper (h_u) and lower (h_d) layers used for a given simulation. Figure S4 and S5 show values of EffCS and the parameter γ for the nine simulations, respectively, while the values of AAWR for the nine benchmark simulations are shown in Fig. A1. The model setup used for the simulations in the main paper are shown in Figs. S4e and S5e.

Figure S6 shows the global SAOD from the GloSSAC dataset (Sect. 2.2.4) in black. To provide an estimate of SAOD for 2024, we use a linear regression to the GloSSAC SAOD between July 2022 and December 2023 (dashed red line), which is extrapolated to cover the year 2024 (solid red line).

40

Section 3.4 states that "Here, we perform a simple correlation analysis between the surface air temperatures and IOD to provide a qualitative illustration of the effects of the 2023 ExpIOD on regional temperatures". The results from our correlation analysis are shown in Figs. S7-S9, and are described below. Figure S7a shows the correlation between the annual mean surface air temperature from the ERA5 reanalysis (Hersbach et al., 2020) and the COBE2 IOD index used in our simulations, over 1980–2024. This time period is generally consistent with the one used for the analysis of recent ExpIOD events by Xie et al. (2025). We use the 1980–2024 time period for the entirety of our correlation analysis. We also tested the correlations between the ERA5 surface air temperatures and a second IOD index, which was derived from the HadISST SST dataset (Rayner et al., 2003) (Fig. S7b). Finally, we also performed the same correlation analysis using the surface air temperatures from the MERRA2 reanalysis (Gelaro et al., 2017). Correlations from that analysis are highly similar to the ERA5-based results, and we will hereafter focus on the ERA5-based correlation analysis. Figure S9 shows the correlation between the ERA5 surface air temperatures and the Nino 3.4 index derived from HadISST SSTs. Four key geographical locations are highlighted across Figs. S7–S9, which correspond to regions where the correlation between surface air temperatures and ENSO is limited (Fig. S9), but correlation with IOD is high (Figs. S7a-b and S8a-b). The four highlighted regions in South America, Europe, Asia and South Australia are labelled SA, EU, AS and AU, respectively. We show the difference between the 2023 and 2022 annual mean surface temperatures in Fig. S7c, while the difference between the 2024 and 2023 annual means are shown in Fig. S7d. All four highlighted regions experienced a considerable rise in surface temperatures in 2023 relative to 2022, with the most prominent rise being in the SA and AU regions. The positive IOD in 2023 progressively decayed into a neutral state by the summer of 2024 (Fig. 3p-r). Surface temperatures declined in 2024, relative to 2023, in the SA region (Fig. S7d), while no significant cooling is noticeable in the other three regions. Importantly, however, the annual mean surface temperatures shown in Fig. S7c-d are influenced by positive IOD in early 2024 (Fig. 3p-r), before the decay of IOD to a neutral state. Therefore, to better examine the effects of IOD on the surface temperatures in these four regions, we performed the same analysis for the ASO season (Fig. S8), which corresponds to the largest 3-month mean contribution to GMST from IOD in 2023 (Fig. 3p-r). In 2024, this three-month period corresponds to an IOD-neutral state. Over the ASO season, all four highlighted regions experienced a considerable rise in surface temperatures in 2023 relative to 2022 (Fig. S8c). Furthermore, a clear decline in surface temperatures is noticeable in all four regions in 2024, compared to 2023 (Fig. S8d).

The figures for the above correlation analyses were generated using the Climate Reanalyzer tool hosted by the University of Maine at https://climatereanalyzer.org/ (Climate Reanalyzer, 2025), with its content available under the Creative Commons Attribution 4.0 International License.

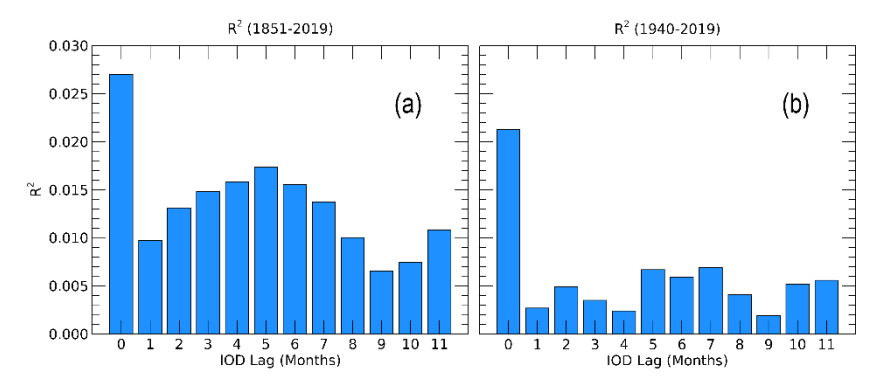


Figure S1: The square of the correlation coefficient (R²) between the lagged IOD index and the time series of residuals, which was obtained by subtracting the 50th percentile modelled GMST from the HadCRUT5 observations. The IOD was removed as a regressor from the model simulation used for this purpose. (a) Values of R² over the 1851–2019 period. (b) Values of R² over 1940–2019.

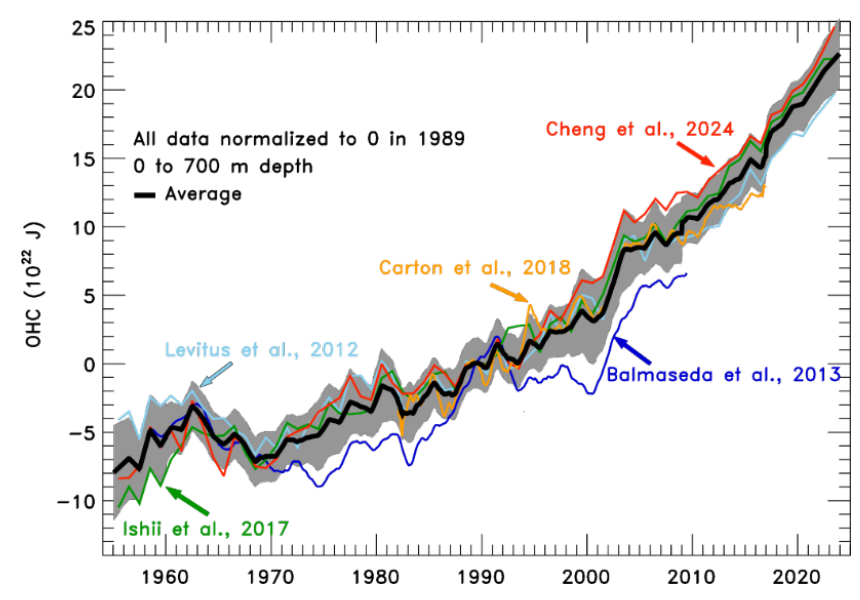


Figure S2: Ocean heat content time series. Colors represent the individual OHC time series, that were used to compute the average OHC time series. The average OHC time series, and the corresponding range of uncertainty is shown by the black line and gray shading, respectively.

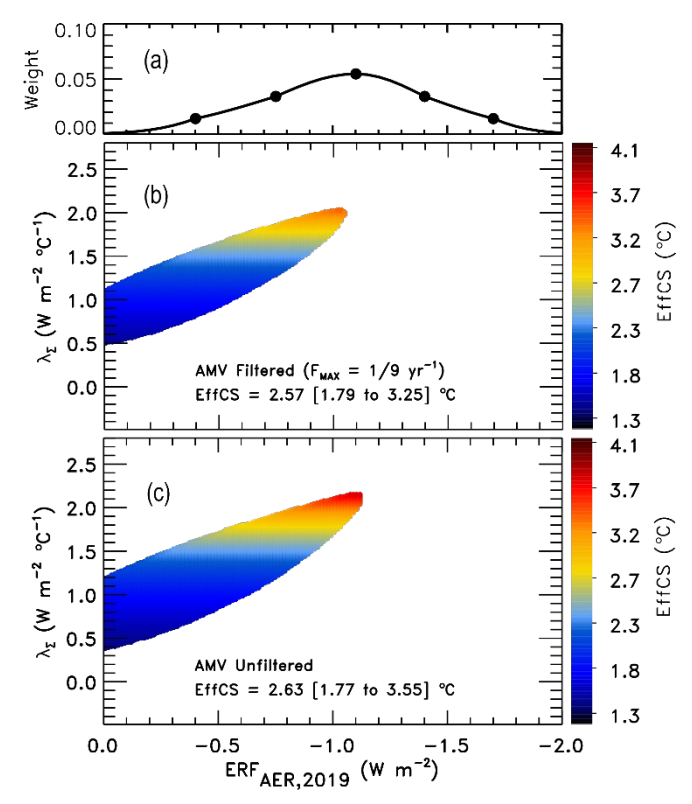


Figure S3: Aerosol weighting method, and computed values of EffCS for the EM–GC ensemble. (a): Asymmetrical Gaussian function used to weight the ensemble. The points marked on the Gaussian represent the center point, the 1σ and 2σ boundaries of the Gaussian (see Sect. 2.7 and Table S3 of Farago et al., (2025)). (b) Values of EffCS as the function of λ_{Σ} and ERF_{AER,2019}. Colors denote specific values of EffCS as indicated by the color bar on the right. EffCS is only shown for those combinations of λ_{Σ} and ERF_{AER,2019}, where all three χ^2 observational constraints are satisfied. The AMV input of the simulation used to produce this panel has been Fourier-filtered to remove frequencies greater than $1/9 \text{ yr}^{-1}$. (c) As in (b), but without a Fourier-filter having been applied to the AMV input. The 50th percentile and the 5–95% range of EffCS from the weighted ensemble are also given on panels (b) and (c).

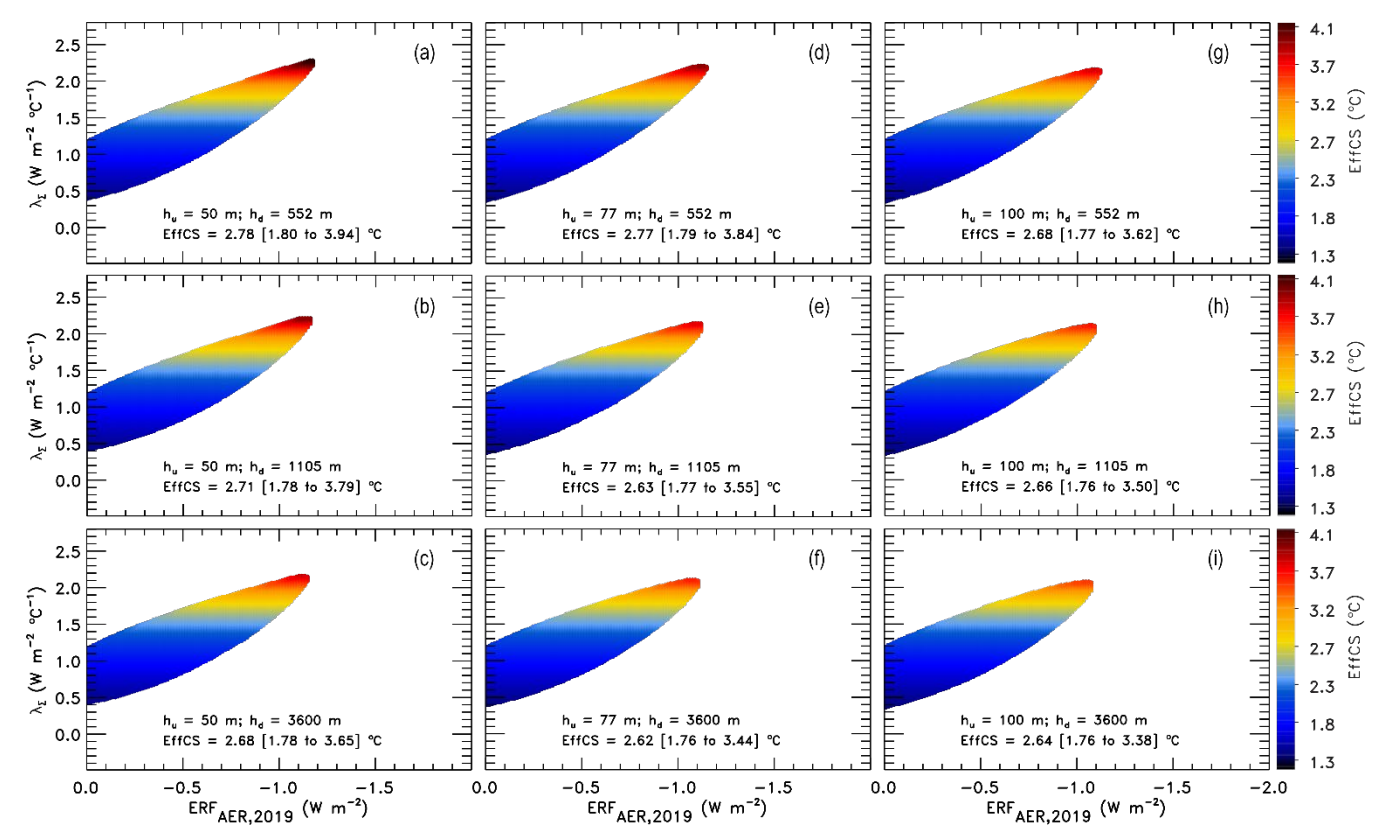


Figure S4: Values of EffCS as the function of climate feedback and ERF $_{AER,2019}$ (Sect. 2.1.2), for nine different combinations of the equivalent depth of the upper (h_u) and lower (h_d) layers of the two-layer EBM. The 50th percentile and the 5–95% range of EffCS from the weighted ensemble are also given on each panel.

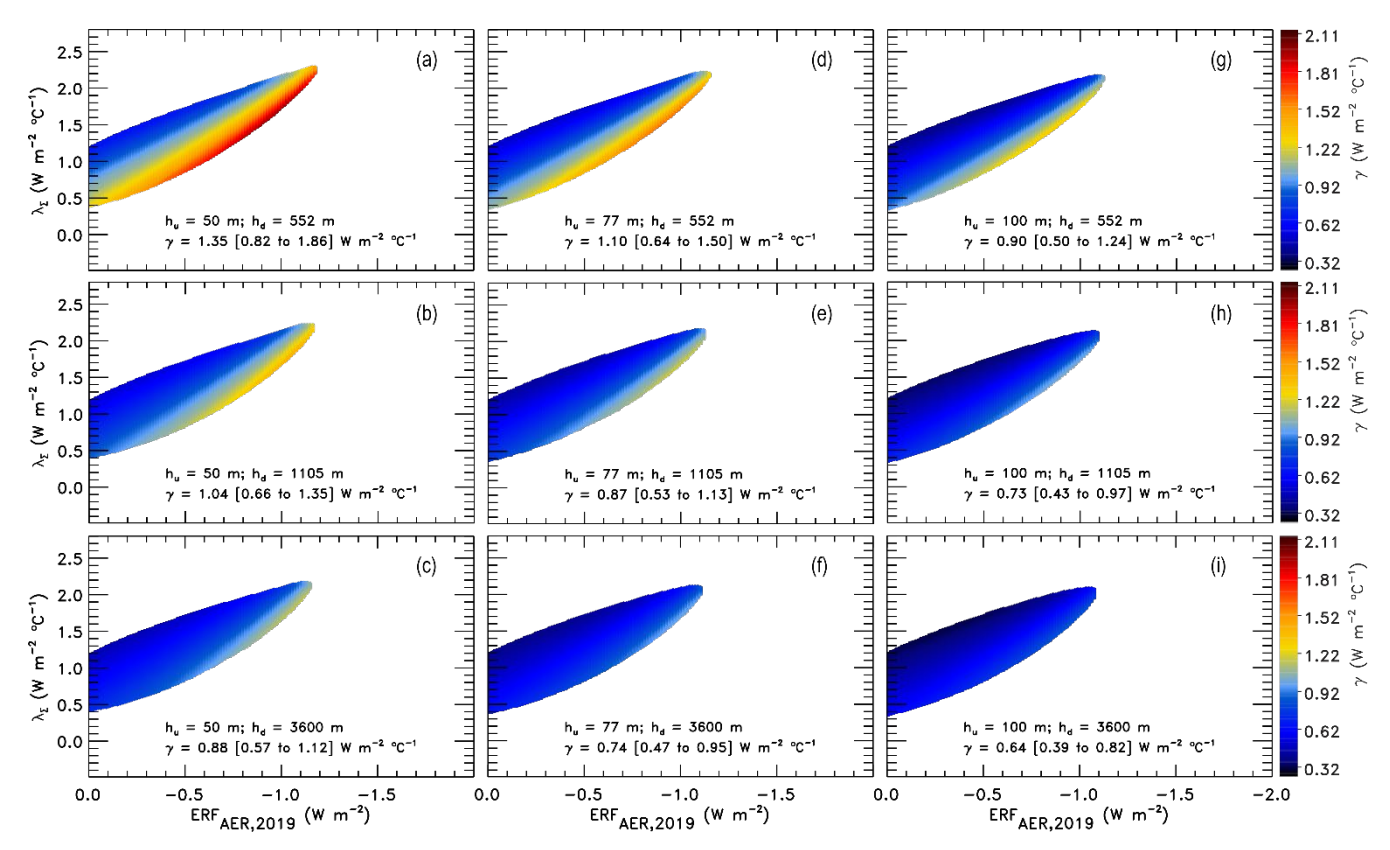


Figure S5: Values of the parameter γ as the function of climate feedback and ERF_{AER,2019} (Sect. 2.1.2), for nine different combinations of the equivalent depth of the upper (h_u) and lower (h_d) layers of the two-layer EBM. The 50th percentile and the 5–95% range of the parameter γ from the weighted ensemble are also given on each panel.

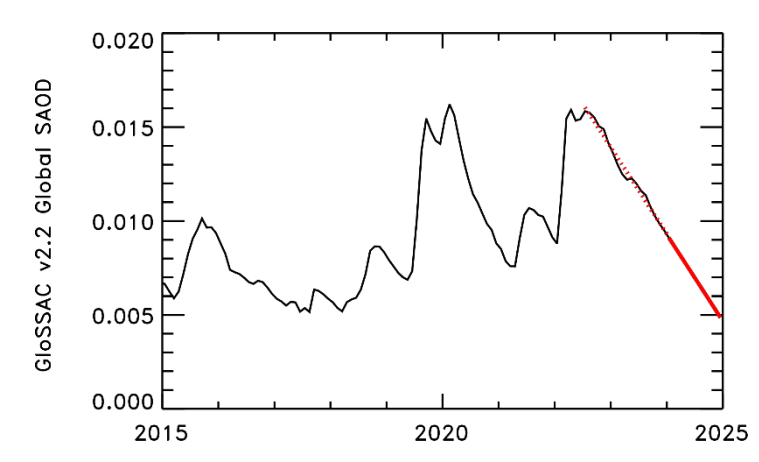


Fig. S6: GloSSAC SAOD (black) and its extension to 2024 (solid red line). The dashed red line represents the linear fit to the observed SAOD between July 2022 and December 2023.

Figure S7: (a) Correlation between the COBE2 IOD index and the annual mean surface temperatures from the ERA5 reanalysis over 1980–2024. Correlations are plotted at a 90% confidence interval. (b) As in (a), but using an IOD index computed from HadISST SSTs. (c) Annual mean surface air temperatures from the ERA5 reanalysis in 2023, relative to 2022. (d) As in (c), but with the difference between the 2024 and 2023 annual mean surface temperatures being shown. Black boxes correspond to four highlighted geographical regions (see text). All plots generated using the Climate Reanalyzer tool hosted by the University of Maine at https://climatereanalyzer.org/ (Climate Reanalyzer, 2025).

ClimateReanalyzer.org | Climate Change Institute | University of Maine

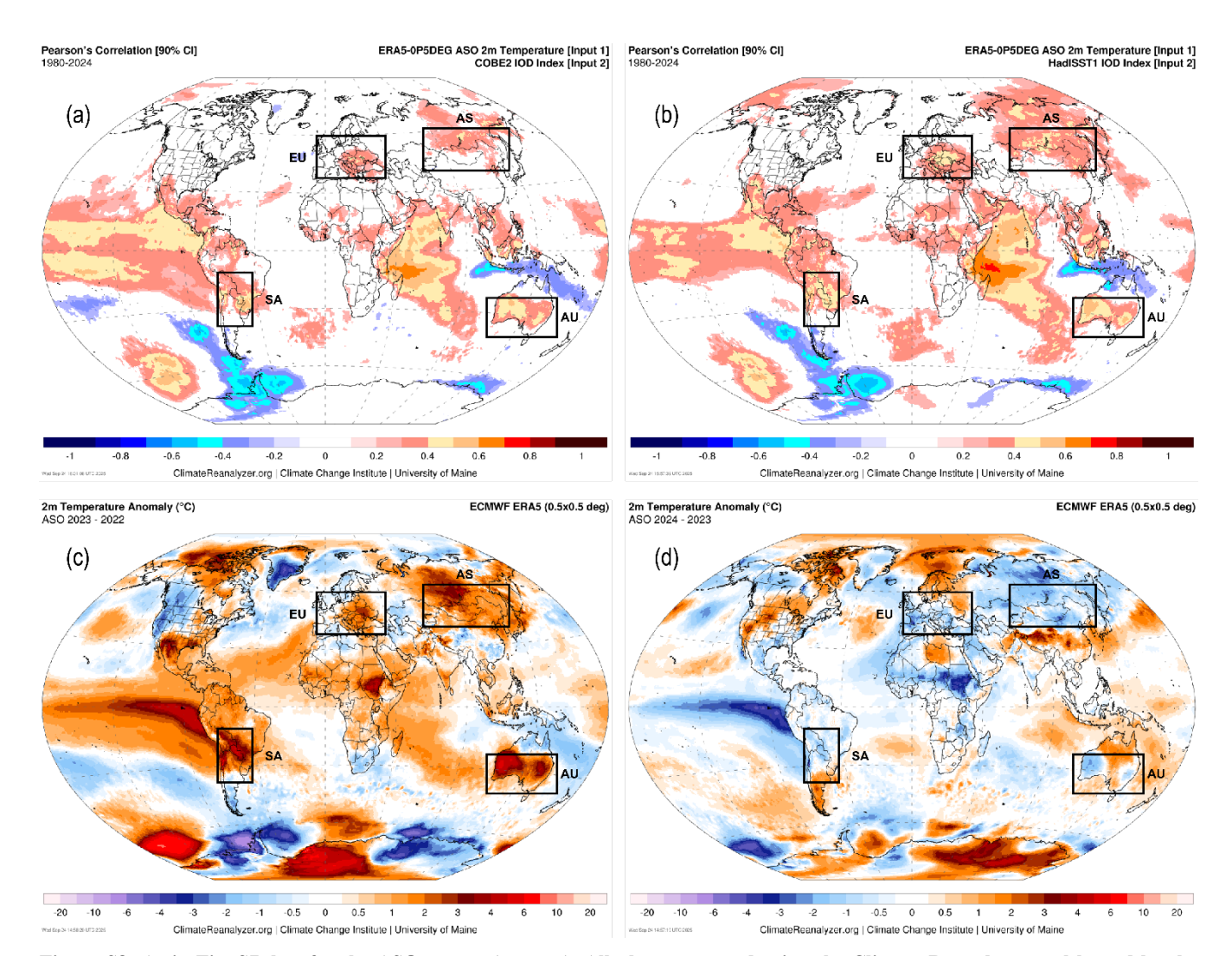


Figure S8: As in Fig. S7, but for the ASO season (see text). All plots generated using the Climate Reanalyzer tool hosted by the University of Maine at https://climatereanalyzer.org/ (Climate Reanalyzer, 2025).

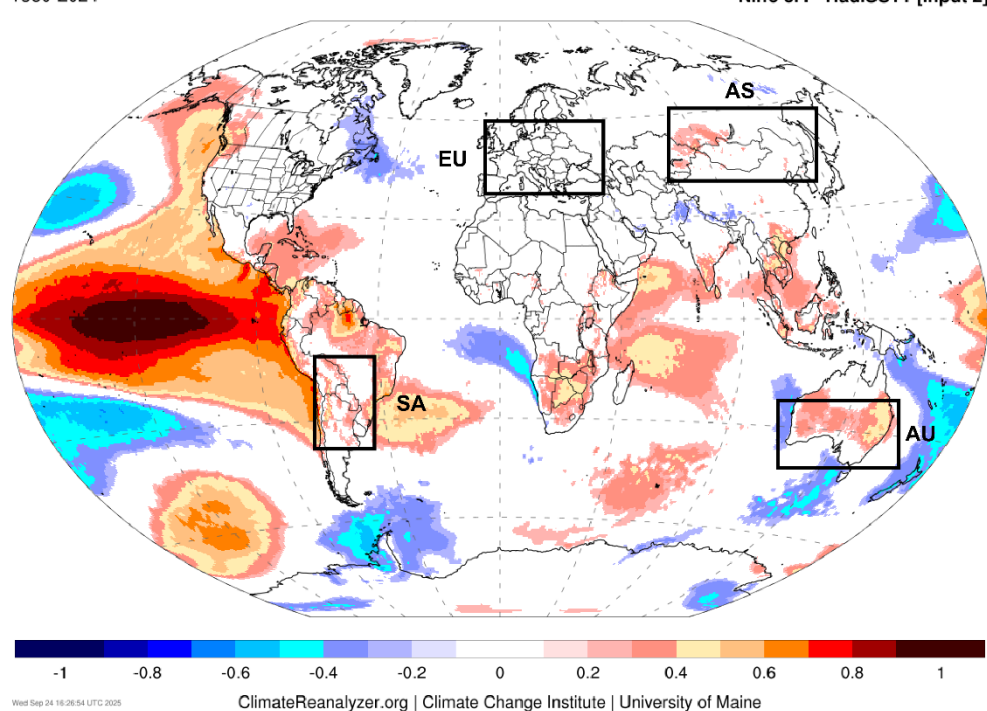


Figure S9: Correlation between the Nino 3.4 index derived from HadISST SSTs, and the annual mean surface temperatures from the ERA5 reanalysis over 1980–2024. As in Fig. S7a, but for the Nino 3.4 index. All plots generated using the Climate Reanalyzer tool hosted by the University of Maine at https://climatereanalyzer.org/ (Climate Reanalyzer, 2025).

120 References

- Balmaseda, M. A., Trenberth, K. E., and Källén, E.: Distinctive climate signals in reanalysis of global ocean heat content, Geophysical Research Letters, 40, 10.1002/grl.50382, 2013.
- Carton, J. A., Chepurin, G. A., and Chen, L.: SODA3: A new ocean climate reanalysis, Journal of Climate, 31, 10.1175/jcli-d-18-0149.1, 2018.
- 125 Cheng, L., Pan, Y., Tan, Z., Zheng, H., Zhu, Y., Wei, W., Du, J., Yuan, H., Li, G., Ye, H., Gouretski, V., Li, Y., Trenberth, K. E., Abraham, J., Jin, Y., Reseghetti, F., Lin, X., Zhang, B., Chen, G., Mann, M. E., and Zhu, J.: IAPv4 ocean temperature and ocean heat content gridded dataset, Earth Syst. Sci. Data, 16, 3517-3546, 10.5194/essd-16-3517-2024, 2024.
 - Climate Reanalyzer: Monthly Reanalysis Correlation Maps and Monthly Reanalysis Maps, Climate Change Institute, University of Maine. Retrieved September 24, 2025., https://climatereanalyzer.org/, 2025.
- Farago, E. Z., McBride, L. A., Hope, A. P., Canty, T. P., Bennett, B. F., and Salawitch, R. J.: AR6 updates to RF by GHGs and aerosols lowers the probability of accomplishing the Paris Agreement compared to AR5 formulations, EGUsphere, 2025, 1-43, 10.5194/egusphere-2025-342, 2025.
 - Gelaro, R., McCarty, W., Suárez, M. J., Todling, R., Molod, A., Takacs, L., Randles, C. A., Darmenov, A., Bosilovich, M. G., Reichle, R., Wargan, K., Coy, L., Cullather, R., Draper, C., Akella, S., Buchard, V., Conaty, A., da Silva, A. M., Gu, W., Kim, G.-K., Koster, R., Lucchesi, R., Merkova, D., Nielsen, J. E., Partyka, G., Pawson, S., Putman, W., Rienecker, M.,

- Schubert, S. D., Sienkiewicz, M., and Zhao, B.: The Modern-Era Retrospective Analysis for Research and Applications, Version 2 (MERRA-2), Journal of Climate, 30, 5419-5454, https://doi.org/10.1175/JCLI-D-16-0758.1, 2017.
- Hersbach, H., Bell, B., Berrisford, P., Hirahara, S., Horányi, A., Muñoz-Sabater, J., Nicolas, J., Peubey, C., Radu, R., Schepers, D., Simmons, A., Soci, C., Abdalla, S., Abellan, X., Balsamo, G., Bechtold, P., Biavati, G., Bidlot, J., Bonavita, M., De Chiara, G., Dahlgren, P., Dee, D., Diamantakis, M., Dragani, R., Flemming, J., Forbes, R., Fuentes, M., Geer, A., Haimberger, L., Healy, S., Hogan, R. J., Hólm, E., Janisková, M., Keeley, S., Laloyaux, P., Lopez, P., Lupu, C., Radnoti, G., de Rosnay, P., Rozum, I., Vamborg, F., Villaume, S., and Thépaut, J.-N.: The ERA5 global reanalysis, Quarterly Journal of the Royal Meteorological Society, 146, 1999-2049, https://doi.org/10.1002/qj.3803, 2020.
- Hope, A. P., McBride, L. A., Canty, T. P., Bennett, B. F., Tribett, W. R., and Salawitch, R. J.: Examining the human influence on global climate using an empirical model, 10.1002/essoar.10504179.1, 2020.
 - Ishii, M., Fukuda, Y., Hirahara, S., Yasui, S., Suzuki, T., and Sato, K.: Accuracy of Global Upper Ocean Heat Content Estimation Expected from Present Observational Data Sets, SOLA, 13, 10.2151/sola.2017-030, 2017.
 - Levitus, S., Antonov, J. I., Boyer, T. P., Baranova, O. K., Garcia, H. E., Locarnini, R. A., Mishonov, A. V., Reagan, J. R., Seidov, D., Yarosh, E. S., and Zweng, M. M.: World ocean heat content and thermosteric sea level change (0-2000m), 1955-2010, Geophysical Research Letters, 39, 10.1029/2012GL051106, 2012.

- McBride, L. A., Hope, A. P., Canty, T. P., Bennett, B. F., Tribett, W. R., and Salawitch, R. J.: Comparison of CMIP6 historical climate simulations and future projected warming to an empirical model of global climate, Earth System Dynamics, 12, 10.5194/esd-12-545-2021, 2021.
- Rayner, N. A., Parker, D. E., Horton, E. B., Folland, C. K., Alexander, L. V., Rowell, D. P., Kent, E. C., and Kaplan, A.: Global analyses of sea surface temperature, sea ice, and night marine air temperature since the late nineteenth century, Journal of Geophysical Research: Atmospheres, 108, https://doi.org/10.1029/2002JD002670, 2003.
 - Xie, M., Wang, J.-Z., Zhang, L., and Chen, Z.: Exceptional Equatorial Extension of Extreme Indian Ocean Dipole Cooling: Shaping Effect From Strong El Niño, Geophysical Research Letters, 52, e2024GL112464, https://doi.org/10.1029/2024GL112464, 2025.